CrossMark

J. Fluid Mech. (2016), *vol.* 790, *pp.* 389–406. © Cambridge University Press 2016
doi:10.1017/jfm.2016.15

Margination of white blood cells: a computational approach by a hydrodynamic phase field model

Wieland Marth[1], **Sebastian Aland**[1] **and Axel Voigt**[1,2,†]

[1]Institute of Scientific Computing, TU Dresden, 01062 Dresden, Germany

[2]Center for Systems Biology Dresden, Pfotenhauerstr. 108, 01307 Dresden, Germany

(Received 8 October 2015; revised 30 November 2015; accepted 5 January 2016)

We numerically investigate margination of white blood cells and demonstrate the dependency on a number of conditions including haematocrit, the deformability of the cells and the Reynolds number. The approach, which is based on a mesoscopic hydrodynamic Helfrich-type model, reproduces previous results, e.g. a decreasing tendency for margination with increasing deformability and a non-monotonic dependency on haematocrit. The consideration of inertia effects, which may be of relevance in various parts of the cardiovascular system, indicates a decreasing tendency for margination with increasing Reynolds number. The effect is discussed by analysing inertial and non-inertial lift forces for single cells under different flow conditions and large-scale two-dimensional simulations of interacting red blood cells and white blood cells in an idealized blood vessel.

Key words: biological fluid dynamics, blood flow

1. Introduction

Various experimental and simulation studies of flowing blood have shown that red blood cells (RBCs) are concentrated in the centre of the blood vessel. This can be explained by a non-inertial lift force, arising from cell–wall and cell–cell hydrodynamic interactions, the high deformability of RBCs and their non-spherical shapes, see e.g. Kumar & Graham (2012) for a recent review. The non-inertial lift force results in a migration of RBCs towards the centre of the vessel and an RBC-free layer near the wall. Differences in size, shape and deformability are assumed to lead to different non-inertial lift forces, which results in a separation of cells with different mechanical properties within the blood vessel. White blood cells (WBCs) have a near-spherical shape and are not very deformable and are therefore mechanically different from RBCs. The non-inertial lift force of WBCs is expected to be much lower than that on RBCs, or even zero in the limit of a rigid-body approximation for WBCs (Goldsmith & Mason 1961; Bretherton 1962). This suggests that WBCs may get marginated to the RBC-free layer near the wall. This effect requires the

† Email address for correspondence: axel.voigt@tu-dresden.de

interaction of RBCs and WBCs and is of utmost importance for a well-functioning immune system, which requires the adhesion of WBCs to the vessel wall.

For low Reynolds numbers the phenomenon is in principle understood. However, in this regime detailed investigations also show a non-trivial dependence of WBC margination on various blood flow properties, such as haematocrit H_t, vessel geometry and RBC aggregation (Pearson & Lipowsky 2000; Abbitt & Nash 2003; Jain & Munn 2009). One example is a pronounced margination within an intermediate range of $H_t \approx$ 0.2–0.3, and reduced WBC margination for lower and higher H_t. Only recently could such behaviour be explained through simulation studies in two dimensions (Fedosov, Fornleitner & Gompper 2012). It is argued that for low H_t, WBC margination turns out to be weak due to a low concentration of RBCs and thus less interaction, while at high H_t WBC margination is attenuated due to interactions of marginated WBCs with RBCs near a wall, which significantly limit the time WBCs spend near a wall. This argumentation is confirmed by 3D simulations in an idealized blood vessel (Fedosov & Gompper 2014; Takeishi *et al.* 2014).

The situation changes, if inertial effects come into play. Now, an inertial lift force is present, which acts on all cells at intermediate-Reynolds-number flows (Geislinger & Franke 2014). As a consequence WBCs also experience a lift force, even in the limit of a rigid-body approximation. This contradicts the simple explanation for WBC margination given above and indeed leads to decreasing margination for an increasing Reynolds number. We vary the Reynolds number, considering values of order 10^{-4}, 10^{-2}, 1 and 10, corresponding to different regions in the cardiovascular system (Formaggiam, Quarteroni & Veneziani 2000). Reynolds numbers of order unity or higher have been reported in large blood vessels, such as arterioles and arteries (Prothero & Burton 1962; Ku 1997), especially if the vessels are constricted due to diseases such as thrombosis (see e.g. Vennemann, Lindken & Westerweel 2007; Bark & Ku 2010).

The paper is organized as follows. In § 2 we first review existing modelling approaches. Next our approach is described in detail. It is based on a Helfrich-type curvature-elastic model (Helfrich 1973). We consider various constraints concerning membrane inextensibility and area conservation for the RBCs and treat WBCs using a rigid-body approximation or as objects with a weakly extensible membrane. We further consider cell–cell interactions and model the fluid flow of the blood plasma and the internal fluids using the incompressible Navier–Stokes equations. We prove thermodynamic consistency of the model and briefly discuss the numerical approach. This approach requires only measurable parameters as input and thus in principle allows for quantitative predictions. However, we will restrict our simulations to two dimensions. The effect of various parameters on the margination of WBCs is discussed in § 3, first reproducing known results for low-Reynolds-number regimes and then analysing the effect of intermediate Reynolds numbers. The decreasing effect of the Reynolds number on WBC margination is discussed in detail and explained by investigations of the inertial lift force on a single RBC and a single WBC. Finally, we draw conclusions in § 4.

2. Methods and models

2.1. *Previous models*

Previous simulation studies, which have been performed to describe WBC margination, are based on strong model assumptions. The simulation approach (Freund 2007) assumes an incompressible Stokes flow, the cells are modelled with a linear elastic

membrane and a global area constraint is enforced. A boundary integral formulation is used for numerical discretization. More recently, a particle-based Lagrangian approach was used (Fedosov *et al.* 2012; Fedosov & Gompper 2014). Here, RBCs and WBCs are described by a network model, where the cells are represented through triangulated surfaces. Penalty terms are used to ensure global volume and global area conservation as well as local area conservation for each surface element. The approach therefore guarantees inextensibility for sufficiently small surface elements. Each membrane point is connected to the fluid through viscous friction. The dynamics of the fluid flow is described by the smoothed dissipative particle dynamics (SDPD) method, an approximation for the Navier–Stokes equations which is only precise, if the particle density is large enough. Furthermore, the incompressibility of the fluid is not guaranteed *a priori* and has to be controlled. In Takeishi *et al.* (2014), a finite element approach is used for the RBCs, which are modelled as biconcave capsules and a Lattice–Boltzmann method for the fluid flow. The problems are coupled through an immersed boundary method.

Our approach is fully continuous and considers RBCs using a Helfrich-type curvature elastic model with an inextensibility constraint. WBCs are modelled either as rigid bodies or again with a Helfrich-type curvature elastic model, but with a constraint allowing for weak extensibility. Furthermore, we will consider the full Navier–Stokes equations to account for inertia effects in the plasma. According to previous studies (N'Dri, Shyy & Tran-Son-Tay 2003) we also consider the internal fluid of the RBCs and WBCs as an incompressible Newtonian fluid, neglecting internal structures and the nucleus in WBCs.

2.2. *Helfrich-type models*

Helfrich-type modelling approaches have been applied to understand the complex motions and shape changes RBCs undergo within a flow field, e.g. tank-treating (TT) and tumbling (TB) motion (Fischer, Stöhr-Liesen & Schmid-Schönbein 1978). Within a low-Reynolds-number regime, the Stokes limit is valid and various numerical approaches have also been considered in this limit to analyse the TT and TB motion (Kraus *et al.* 1996; Biben & Misbah 2003; Beaucourt *et al.* 2004; Biben, Kassner & Misbah 2005; Veerapaneni *et al.* 2009; Ghigliotti, Biben & Misbah 2010; Kim & Lai 2010; Sohn *et al.* 2010; Zhao & Shaqfeh 2011). All models consider a membrane-free energy

$$\mathscr{E} = \int_\Gamma \frac{1}{2} b_N (H - H_0)^2 \,\mathrm{d}\Gamma, \tag{2.1}$$

with membrane $\Gamma(t)$, mean curvature H, spontaneous curvature H_0 and normal bending rigidity b_N. Lagrange multipliers are used to enforce a global area constraint or the stronger inextensibility constraint. The jump condition for the fluid stress tensor $\boldsymbol{S} = S_{0,i} = -p\boldsymbol{I} + \nu_{0,i}\boldsymbol{D}$, with pressure p, fluid viscosity ν_0, cell viscosity ν_i and deformation tensor $\boldsymbol{D} = \nabla \boldsymbol{v} + (\nabla \boldsymbol{v})^{\mathrm{T}}$, with velocity $\boldsymbol{v}$, along the membrane then reads

$$[\boldsymbol{S}\cdot\boldsymbol{n}]_\Gamma = \frac{\delta \mathscr{E}}{\delta \Gamma} + \lambda_{global} H\boldsymbol{n} \quad \text{global area constraint,} \tag{2.2}$$

$$[\boldsymbol{S}\cdot\boldsymbol{n}]_\Gamma = \frac{\delta \mathscr{E}}{\delta \Gamma} + \lambda_{local} H\boldsymbol{n} + \nabla_\Gamma \lambda_{local} \quad \text{local inextensibility constraint,} \tag{2.3}$$

with outer normal $\boldsymbol{n}$ and the surface gradient $\nabla_\Gamma = \boldsymbol{P}\nabla$, where $\boldsymbol{P} = \boldsymbol{I} - \boldsymbol{n}\otimes\boldsymbol{n}$ denotes the projection operator. Index 0 thereby denotes the fluid phase and index i the cell

phase. The Lagrange multipliers λ_{global} and λ_{local} are functionals of the fluid velocity $\boldsymbol{v}$ and are obtained by requiring $\mathrm{d}/\mathrm{d}t \int_\Gamma \mathrm{d}\Gamma = \int_\Gamma H\boldsymbol{v}\cdot\boldsymbol{n}\,\mathrm{d}\Gamma = 0$ for the global area constraint and $\nabla_\Gamma \cdot \boldsymbol{v} = 0$ along $\Gamma(t)$ for the local inextensibility constraint. The jump condition for the velocity reads $[\boldsymbol{v}]_\Gamma = 0$.

The linearity of the Stokes problem allows for efficient decoupled algorithms to solve for the Lagrange multipliers (Biben & Misbah 2003; Sohn *et al.* 2010; Zhao & Shaqfeh 2011). However, in regimes with the Reynolds number being of order unity or higher, the Stokes limit is at least questionable. Modelling approaches, which consider inertia effects, have been introduced recently (Laadhari, Saramito & Misbah 2012; Salac & Miksis 2012; Aland *et al.* 2014). All have found that the classical TB behaviour is no longer observed at moderate Reynolds numbers. As such, a suppression of TB motion could have far reaching consequences also for the interaction of RBCs and thus also the margination of WBCs. In the following, we will consider the full Navier–Stokes equations, which read inside and outside the RBCs

$$\rho(\partial_t \boldsymbol{v} + \boldsymbol{v}\cdot\nabla\boldsymbol{v}) - \nabla\cdot\boldsymbol{S} = 0, \tag{2.4}$$

$$\nabla\cdot\boldsymbol{v} = 0, \tag{2.5}$$

with density $\rho = \rho_{0,i}$. The global area constraint can be treated explicitly, which was e.g. used by Bonito, Nochetto & Pauletti (2011) within a front tracking method, proposed by Du, Li & Liu (2007) and used by Haußer *et al.* (2013) and Marth & Voigt (2014) for a phase-field model and also considered in Salac & Miksis (2011) for a level-set approach. The local inextensibility constraint is more delicate and leads to additional nonlinearities, which are so far only considered within a level-set approach in Salac & Miksis (2011), Laadhari *et al.* (2012) and within a phase field approximation in Aland *et al.* (2014). These models predominantly consider only one cell or simple test cases with more cells, using one level-set or phase field function for all cells. We will demonstrate, that this approach can lead to non-physical behaviour in more complex situations. We further like to distinguish between RBCs and WBCs having different properties, which can more naturally be considered by using different functions to describe different cells. It therefore will be the main modelling contribution to extent the described approaches in Aland *et al.* (2014) to also model interactions of cells in an efficient way.

We will consider WBCs using two different approaches. The first models WBCs as a rigid body with a spherical shape using the fluid particle dynamics (FPD) approach (Tanaka & Araki 2000), and the second accounts again for a Helfrich-type energy equation (2.1) with the jump condition for the fluid stress tensor described by

$$[\boldsymbol{S}\cdot\boldsymbol{n}]_\Gamma = \frac{\delta\mathscr{E}}{\delta\Gamma} + \frac{c}{2}(\mathscr{A}^0 - \mathscr{A}(\Gamma))H\boldsymbol{n} \quad \text{weak global area constraint,} \tag{2.6}$$

with penalty parameter c and initial and desired cell area $\mathscr{A}^0$ and $\mathscr{A}(\Gamma) = \int_\Gamma \mathrm{d}\Gamma$, respectively. Appropriately choosing c allows for moderate changes in area and thus an effective weak extensibility. The internal fluid of the WBCs are again considered as an incompressible Newtonian fluid, but with a larger viscosity as for the RBCs.

2.3. *Hydrodynamic phase field models*

The method introduces auxiliary phase fields ϕ_i that distinguish the inside and the outside of each cell $i = 1, \ldots, n$. The inside and the outside are separated from each

other by a diffuse layer, which marks the membrane. The phase field variables are defined as

$$\phi_i(t, \boldsymbol{x}) := \tanh\left(\frac{r_i(t, \boldsymbol{x})}{\sqrt{2}\epsilon}\right), \tag{2.7}$$

where ϵ characterizes the thickness of the diffuse interface and $r_i(t, \boldsymbol{x})$ denotes the signed-distance function between $\boldsymbol{x} \in \Omega$ and its nearest point on $\Gamma_i(t)$ the membrane of cell i. Depending on r_i, we label the inside with $\phi_i \approx 1$ and the outside with $\phi_i \approx -1$. $\Gamma_i(t)$ is then implicitly defined by the zero level set of ϕ_i. The cell phase can thus be defined as $\phi_{cell} \approx 1$ with $\phi_{cell} = \max_{\boldsymbol{x}\in\Omega}(\phi_1, \ldots, \phi_n)$ and the fluid phase as $\phi_0 = -\phi_{cell} \approx 1$. In the same way we define the RBCs phase ϕ_{RBCs}.

The dynamics are now governed by equations that couple these phase fields to the actual physical degrees of freedom. For WBCs, if considered as rigid bodies, the shape is a sphere and its velocity defined as the average fluid velocity inside

$$\boldsymbol{v}_i(t) = \frac{\displaystyle\int_\Omega \psi_i(t, \boldsymbol{x})\boldsymbol{v}\,\mathrm{d}\Omega}{\displaystyle\int_\Omega \psi_i(t, \boldsymbol{x})\,\mathrm{d}\Omega}, \tag{2.8}$$

with $\psi_i(t, \boldsymbol{x}) = 0.5(\phi_i(t, \boldsymbol{x}) + 1)$. The motion of the WBC can then be described by $\boldsymbol{x}_i(t + \Delta t) = \boldsymbol{x}_i(t) + \Delta t \boldsymbol{v}_i(t)$, with $\boldsymbol{x}_i(t)$ the centre of mass of the WBC and Δt the simulation time step (see Tanaka & Araki 2000). In all other cases we consider the diffuse non-dimensional Helfrich energies

$$\mathscr{E}_i(\phi_i) = \frac{1}{2Re\,Be_i}\int_\Omega \frac{1}{\epsilon}\left(\epsilon\Delta\phi_i - \frac{1}{\epsilon}(\phi_i^2 - 1)(\phi_i + H_0)\right)^2 \mathrm{d}\Omega, \tag{2.9}$$

with Reynolds number $Re = \rho UL/\nu_0$ and bending capillary numbers $Be_i = (4\sqrt{2}/3)(\nu_0 UL^2/b_{N,i})$, where U denotes a characteristic velocity, L a characteristic length and $b_{N,i}$ the bending rigidity of cell i. In Du *et al.* (2005) formal convergence for $\epsilon \to 0$ to the non-dimensional form of the sharp interface energy in (2.1) is shown.

Instead of a direct extension of the models in Aland *et al.* (2014), which considers an L^2-gradient flow for ϕ_i and enforces a volume and local or global area constraint by Lagrange multipliers, we here introduce a H^{-1} gradient flow. This directly ensures volume conservation and only area constraint have to be considered. They are treated as a global area constraint using a penalty approach. Such an approach was already considered for one cell, but without flow interactions, in Campelo & Hernández-Machado (2007). It has the advantage to keep the equations local. We introduce the non-dimensional penalty energies

$$\mathscr{E}_{i,area}(\phi_i) = \frac{c_i}{2Re\,Be_i}(\mathscr{A}_i^0 - \mathscr{A}(\phi_i))^2, \tag{2.10}$$

with penalty parameters c_i, with different values for RBCs and WBCs to ensure global area conservation and weak extensibility, respectively. The initial and desired area of cell i are denoted by $\mathscr{A}_i^0$ and $\mathscr{A}(\phi_i) = \int_\Omega (\epsilon/2)|\nabla\phi_i|^2 + (1/4\epsilon)(\phi_i^2 - 1)^2\,\mathrm{d}\Omega$, respectively. The last term converges to $(2\sqrt{2}/3)\int_{\Gamma_i}\mathrm{d}\Gamma$ if $\epsilon \to 0$ (see Du, Liu & Wang 2006). The penalty energy therefore corresponds to the penalty term considered in (2.6). In case of an enforced stronger local inextensibility constraint for the RBCs,

the penalty term helps to control the accumulation of errors, as shown in Du *et al.* (2006) and Aland *et al.* (2014).

In addition, we require an interaction energy $\mathscr{E}_{int}$, to be defined below, such that the overall energy can be written as

$$\mathscr{E}(\phi_1, \dots, \phi_n) = \sum_{i=1}^{n} (\mathscr{E}_i(\phi_i) + \mathscr{E}_{i,area}(\phi_i)) + \mathscr{E}_{int}(\phi_1, \dots, \phi_n) \tag{2.11}$$

and the evolution equations for ϕ_i read

$$\partial_t \phi_i + \boldsymbol{v} \cdot \nabla \phi_i = \gamma \Delta \phi_i^{\natural}, \tag{2.12}$$

with a small positive mobility coefficient γ and the non-dimensional chemical potentials

$$\phi_i^{\natural} = \frac{\delta \mathscr{E}(\phi_1, \dots, \phi_n)}{\delta \phi_i} = \frac{\delta \mathscr{E}_i(\phi_i)}{\delta \phi_i} + \frac{\delta \mathscr{E}_{i,area}(\phi_i)}{\delta \phi_i} + \frac{\delta \mathscr{E}_{int}(\phi_1, \dots, \phi_n)}{\delta \phi_i}. \tag{2.13}$$

We obtain

$$\left.\begin{aligned} \frac{\delta \mathscr{E}_i}{\delta \phi_i} = \frac{1}{Re\, Be_i} \psi_i, \quad \psi_i = \Delta \mu_i - \frac{1}{\epsilon^2}(3\phi_i^2 + 2H_0\phi - 1)\mu_i, \\ \mu_i = \epsilon \Delta \phi_i - \frac{1}{\epsilon}(\phi_i^2 - 1)(\phi_i + H_0). \end{aligned}\right\} \tag{2.14}$$

The penalty terms read

$$\frac{\delta \mathscr{E}_{i,area}}{\delta \phi_i} = \frac{c_i}{Re\, Be_i} \kappa_i (\mathscr{A}_i^0 - \mathscr{A}(\phi_i)), \quad \kappa_i = \epsilon \Delta \phi_i - \frac{1}{\epsilon}(\phi_i^2 - 1)\phi_i. \tag{2.15}$$

Now, we have to consider the interaction terms. Interaction in principle is computationally costly, as it turns the problem into a nonlocal one and requires the coupling of all phase field variables $\phi_1, \dots, \phi_n$ and computations of the distance between cells. We here consider only steric interactions to prevent coalescence or overlapping of cells and model the short range repulsion by a Gaussian potential, which in the sharp interface description reads

$$\mathscr{E}_{i,int}(\Gamma_1, \dots, \Gamma_n) = \sum_{\substack{j=1 \\ j \neq i}}^{n} \alpha \int_{\Gamma_i} w_j \, \mathrm{d}\Gamma, \quad \text{with } w_j(\boldsymbol{x}) = \exp\left(-\frac{r_j^2(\boldsymbol{x})}{\epsilon^2}\right), \tag{2.16}$$

where w_j is an interaction function and describes the influence of cell j on its environment. The interaction parameter $\alpha > 0$ determines the strength of the repulsive interaction between cell i and cell j with respect to the evolution of cell i. Using (2.7), the signed distance function r_j can be computed within the diffuse interface region as

$$r_j = -\frac{\epsilon}{\sqrt{2}} \ln \frac{1 + \phi_j}{1 - \phi_j} \quad \forall \boldsymbol{x} : |\phi_j(\boldsymbol{x})| < 1. \tag{2.17}$$

We thus can write the short-range interaction function w_j as

$$w_j = \begin{cases} \exp\left(-\frac{1}{2}\left(\ln \frac{1 + \phi_j}{1 - \phi_j}\right)^2\right) & \text{if } |\phi_j(\boldsymbol{x})| < 1 \\ 0 & \text{otherwise} \end{cases} \tag{2.18}$$

and consider the interaction potential within the phase-field description, which reads in non-dimensional form

$$\mathscr{E}_{i,int}(\phi_1, \ldots, \phi_n) = \frac{1}{Re\, In} \int_\Omega B(\phi_i) \sum_{\substack{j=1 \\ j\neq i}}^{n} w_j \, \mathrm{d}\Omega, \tag{2.19}$$

with $B(\phi_i) = (1/\epsilon)(\phi_i^2 - 1)^2$ being non-zero only within the diffuse interface around Γ_i and $In = (4\sqrt{2}/3)(\nu_0 U/\alpha)$ the interaction number. The interaction energy thus reads

$$\mathscr{E}_{int}(\phi_1, \ldots, \phi_n) = \sum_{i=1}^{n} \mathscr{E}_{i,int}(\phi_1, \ldots, \phi_n) \tag{2.20}$$

and we obtain

$$\frac{\delta \mathscr{E}_{int}(\phi_1, \ldots, \phi_n)}{\delta \phi_i} = \frac{1}{Re\, In} \left(B'(\phi_i) \sum_{\substack{j=1 \\ j\neq i}}^{n} w_j + w_i' \sum_{\substack{j=1 \\ j\neq i}}^{n} B(\phi_j) \right), \tag{2.21}$$

with

$$w_i' = \begin{cases} \dfrac{2}{\phi_i^2 - 1} \ln \dfrac{1+\phi_i}{1-\phi_i} \exp\left(-\dfrac{1}{2} \left(\ln \dfrac{1+\phi_i}{1-\phi_i} \right)^2 \right) & \text{if } |\phi_i(\boldsymbol{x})| < 1 \\ 0 & \text{otherwise.} \end{cases} \tag{2.22}$$

Figure 1 gives a schematic illustration of the interaction terms. The algorithm considers only these cells, for which the diffuse interfaces overlap. All other cells do not contribute to the interaction. In addition, the most expensive part, computing the distance between cells, has been avoided, as this information is already contained in the phase field description of the cells. The approach thus scales with n, the number of cells. Similar ideas to model interactions within phase field approaches have been considered in Zhang, Das & Du (2009) and Gu, Wang & Gunzburger (2014). However, only for the interaction of one cell with a fixed substrate.

The non-dimensional Navier–Stokes equation reads

$$\rho(\partial_t \boldsymbol{v} + \boldsymbol{v} \cdot \nabla \boldsymbol{v}) + \nabla p - \frac{1}{Re} \nabla \cdot (\nu \boldsymbol{D}) = \sum_{i=1}^{n} \phi_i^\sharp \nabla \phi_i, \tag{2.23}$$

$$\nabla \cdot \boldsymbol{v} = 0, \tag{2.24}$$

with $\rho = 1$ and $\nu = (1 - \phi_{cell}/2) + \sum_{i=1}^{n} (\nu_i/\nu_0)((\phi_i + 1)/2)$. Different densities could be handled in a similar way but are omitted here for simplicity.

To enforce the local inextensibility constraint for the RBCs, we follow the approach of model B in Aland *et al.* (2014). The nonlinear evolution equations for ϕ_i remain, only the Navier–Stokes equation has to be extended and now reads

$$\rho(\partial_t \boldsymbol{v} + \boldsymbol{v} \cdot \nabla \boldsymbol{v}) + \nabla p - \frac{1}{Re} \nabla \cdot (\nu \boldsymbol{D}) = \sum_{i=1}^{n} \phi_i^\sharp \nabla \phi_i + \nabla \cdot \left(\frac{|\nabla \phi_{RBCs}|}{2} \boldsymbol{P} \lambda_{local} \right), \tag{2.25}$$

$$\nabla \cdot \boldsymbol{v} = 0, \tag{2.26}$$

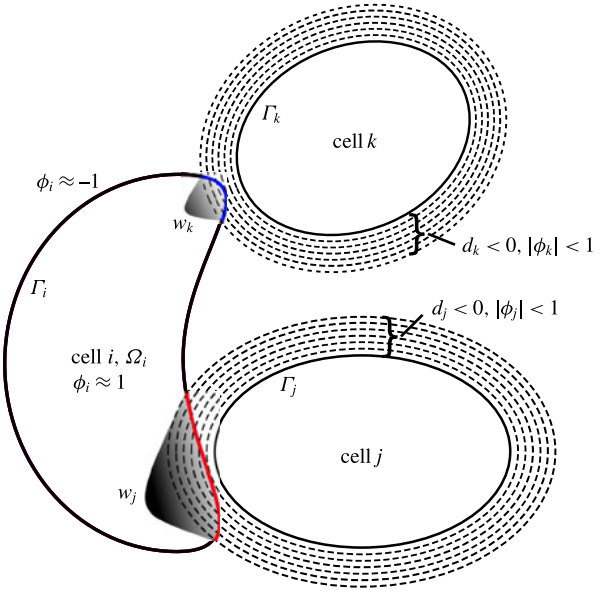

FIGURE 1. (Colour online) The red and blue coloured parts of Γ_i are in contact with the interfaces of cell j and cell k (dashed contours around those cells), where the signed functions r_j and r_k can be calculated and thus also the interaction functions w_j and w_k. They do not vanish in the overlapping regions.

with a Lagrange multiplier λ_{local} for which we introduce the additional equation

$$\xi\epsilon^2\nabla\cdot(\phi_{RBCs}^2\nabla\lambda_{local}) + \frac{|\nabla\phi_{RBCs}|}{2}\boldsymbol{P}:\nabla\boldsymbol{v} = 0, \tag{2.27}$$

with $\xi > 0$ a parameter independent of ϵ. For $\epsilon \to 0$ we obtain $\Delta\lambda_{local} = 0$ away from Γ_{RBCs} and $\boldsymbol{P}:\nabla\boldsymbol{v} = \nabla_\Gamma\cdot\boldsymbol{v} = 0$ near Γ_{RBCs}, which was shown in Aland *et al.* (2014) for $n = 1$.

2.4. *Thermodynamic consistency*

The proposed system of equations (2.12) and (2.13) for $i = 1, \ldots, n$ and (2.23) and (2.24) or (2.25)–(2.27) fulfill thermodynamic consistency. To show this, we consider the kinetic energy $\mathscr{E}_{kin} = \int \boldsymbol{v}^2$ with constant density $\rho = 1$ and the cell energy $\mathscr{E}$ and show that the time derivative is less than or equal to zero:

$$\dot{\mathscr{E}}_{tot}(\boldsymbol{v}, \phi_1, \ldots, \phi_n) = \dot{\mathscr{E}}_{kin} + \dot{\mathscr{E}} = \int \boldsymbol{v}\boldsymbol{v}_t + \sum_{i=1}^{n} \phi_i^\sharp \partial_t\phi_i \,\mathrm{d}\boldsymbol{x}, \tag{2.28}$$

with

$$\partial_t\phi_i = -\boldsymbol{v}\cdot\nabla\phi_i + \gamma\Delta\phi_i^\sharp, \tag{2.29}$$

$$\partial_t\boldsymbol{v} = -(\boldsymbol{v}\cdot\nabla)\boldsymbol{v} - \nabla p + \frac{1}{Re}\nabla\cdot(\nu\boldsymbol{D}) + \sum_{i=1}^{n}\phi_i^\sharp\nabla\phi_i + \nabla\cdot\left(\frac{|\nabla\phi_{RBCs}|}{2}\boldsymbol{P}\lambda_{local}\right), \tag{2.30}$$

which yields

$$\begin{aligned}
&\dot{\mathscr{E}}_{tot}(\boldsymbol{v}, \phi_1, \ldots, \phi_n) \\
&= \int \boldsymbol{v} \cdot \left(-(\boldsymbol{v} \cdot \nabla)\boldsymbol{v} - \nabla p + \frac{1}{Re} \nabla \cdot (\nu \boldsymbol{D}) + \sum_{i=1}^{n} \phi_i^{\natural} \nabla \phi_i + \nabla \cdot \left(\frac{|\nabla \phi_{RBCs}|}{2} \boldsymbol{P} \lambda_{local} \right) \right) \\
&\quad + \sum_{i=1}^{n} \phi_i^{\natural} (-\boldsymbol{v} \cdot \nabla \phi_i + \gamma \Delta \phi_i^{\natural}) \, \mathrm{d}\boldsymbol{x} \quad \text{(partial integration, use } \nabla \cdot \boldsymbol{v} = 0) \\
&= \int -\frac{1}{Re} |\nabla \boldsymbol{v}|^2 - \gamma \sum_{i=1}^{n} |\nabla \phi_i^{\natural}|^2 - \left(\nabla \boldsymbol{v} : \frac{|\nabla \phi_{RBCs}|}{2} \boldsymbol{P} \right) \lambda_{local} \, \mathrm{d}\boldsymbol{x} \\
&\quad \text{(use (2.27) and partial integration)} \\
&= \int -\frac{1}{Re} |\nabla \boldsymbol{v}|^2 - \gamma \sum_{i=1}^{n} |\nabla \phi_i^{\natural}|^2 - \xi \epsilon^2 \phi_{RBCs}^2 |\nabla \lambda_{local}|^2 \, \mathrm{d}\boldsymbol{x} \\
&\leqslant 0, \qquad (2.31)
\end{aligned}$$

where we have used the identity $\boldsymbol{v} \times (\nabla \times \boldsymbol{v}) = \nabla(|\boldsymbol{v}|^2) - (\boldsymbol{v} \cdot \nabla)\boldsymbol{v}$ from which follows that $\int \boldsymbol{v} \cdot (-\boldsymbol{v} \cdot \nabla \boldsymbol{v}) = 0$.

2.5. *Numerical approach*

Time discretization. In order to discretize in time, we explore an operator splitting approach. In an iterative process, we first solve the flow problem and substitute its solution into the phase-field equations, which are then solved separately with a parallel splitting method. We split the time interval $I = [0, T]$ into equidistant time instants $0 = t_0 < t_1 < \cdots$ and define the time steps $\tau := t_{n+1} - t_n$. Of course, adaptive time steps may also be used. We define the discrete time derivative $\mathrm{d}_t \cdot^{n+1} := (\cdot^{n+1} - \cdot^n)/\tau$, where the upper index denotes the time step number and e.g. $\boldsymbol{v}^n := \boldsymbol{v}(t_n)$ is the value of $\boldsymbol{v}$ at time t_n. For each system, a semi-implicit time discretization is used, which together with an appropriate linearization of the involved nonlinear terms leads to a set of linear systems in each time step.

Space discretization. We apply the finite element method to discretize in space, where a P^2/P^1 Taylor–Hood element is used for the flow problem, all other quantities are discretized in space using P^2 elements. In each time step we solve the following.

(i) The flow problem for $\boldsymbol{v}^{n+1}$, p^{n+1} and λ_{local}^{n+1}

$$\begin{aligned}
\mathrm{d}_t \boldsymbol{v}^{n+1} + (\boldsymbol{v}^n \cdot \nabla)\boldsymbol{v}^{n+1} \;=\; & -\nabla p^{n+1} + \frac{1}{Re} \nabla \cdot (\nu^n \boldsymbol{D}^{n+1}) \\
& + \sum_{i=1}^{n} \phi_i^{\natural n} \nabla \phi_i^n + \nabla \cdot \left(\frac{|\nabla \phi_{RBCs}^n|}{2} \boldsymbol{P}^n \lambda_{local}^{n+1} \right), \qquad (2.32)
\end{aligned}$$

$$\nabla \cdot \boldsymbol{v}^{n+1} = 0, \qquad (2.33)$$

$$\xi \epsilon^2 \nabla \cdot ((\phi_{RBCs}^n)^2 \nabla \lambda_{local}^{n+1}) + \frac{|\nabla \phi_{RBCs}^n|}{2} \boldsymbol{P}^n : \nabla \boldsymbol{v}^{n+1} = 0, \qquad (2.34)$$

where $\nu^n = \nu(\phi^n)$ and $\boldsymbol{P}^n = \boldsymbol{I} - (\nabla \phi^n \otimes \nabla \phi^n / |\nabla \phi^n|^2)$.

(ii) The phase field equations for ϕ_i^{n+1}, $i = 1, \dots, n$

$$\mathrm{d}_t \phi_i^{n+1} + \boldsymbol{v}^{n+1} \cdot \nabla \phi_i^{n+1} = \gamma \Delta \phi_i^{\wr n+1}, \tag{2.35}$$

$$\begin{aligned} \phi_i^{\wr n+1} = {} & \frac{1}{Re\, Be_i} \psi_i^{n+1} + \frac{c_i}{Re\, Be_i} (\mathscr{A}_{0,i} - \mathscr{A}(\phi_i^n)) \kappa_i^n \\ & + \frac{1}{Re\, In} \left(B'(\phi_i^n) \sum_{\substack{j=1 \\ j \neq i}}^{n} w_j^n + w_i'^n \sum_{\substack{j=1 \\ j \neq i}}^{n} B(\phi_j^n) \right), \end{aligned} \tag{2.36}$$

$$\psi_i^{n+1} = \Delta \mu_i^{n+1} - \frac{1}{\epsilon^2} (3(\phi_i^{n+1})^2 + 2H_0 \phi_i^{n+1} - 1) \mu_i^{n+1}, \tag{2.37}$$

$$\mu_i^{n+1} = \epsilon \Delta \phi_i^{n+1} - \frac{1}{\epsilon} ((\phi_i^{n+1})^2 - 1)(\phi_i^{n+1} + H_0), \tag{2.38}$$

with $\kappa_i^n = -\epsilon \Delta \phi_i^n + (1/\epsilon)((\phi_i^n)^2 - 1)\phi_i^n$. We linearize the nonlinear terms by a Taylor expansion of order one, e.g. $((\phi_i^{n+1})^2 - 1)\phi_i^{n+1} = ((\phi_i^n)^2 - 1)\phi_i^n + (3(\phi_i^n)^2 - 1)(\phi_i^{n+1} - \phi_i^n)$.

Implementation. The fully discretized system of partial differential equations is implemented using the adaptive finite element toolbox AMDiS (Vey & Voigt 2007; Witkowski *et al.* 2015). We use an adaptively refined triangular mesh $\mathscr{T}_h$ with a high resolution along the cell membranes to guarantee at least five grid points across the diffuse interface. We further conduct a shared memory OPENMP parallelization, to solve the phase field evolutions via a parallel splitting method. Each linear system of equations is solved using the direct unsymmetric multifrontal method UMFPACK. For more details we refer to Ling *et al.* (2015).

3. Results and discussion

We study WBC margination for different WBC stiffnesses, different haematocrit values and different Reynolds numbers. We consider a blood vessel of thickness 20 μm and length 40 μm with periodic conditions on the inflow and outflow. The relatively small length results from compromising computational efficiency and physical accuracy and has been obtained through detailed investigations on the influence of the periodicity on WBC margination. We consider RBCs with perimeter 22 μm, area 19.5 μm^2, bending rigidity $b_{N,RBC} = 2 \times 10^{-19}$ J, viscosity $\nu_{RBC} = 1 \times 10^{-3}$ Pa s. WBCs are initially set to be circular with a radius of 5 μm. They have a viscosity $\nu_{WBC} = 50 \times 10^{-2}$ Pa s. In order to study the influence of the stiffness of the WBCs, we consider three types: soft WBCs with $b_{N,WBC} = 2 \times 10^{-19}$ J, hard WBCs with $b_{N,WBC} = 2 \times 10^{-18}$ J and rigid WBCs. The interaction strength is constant between all cell types and reads $\alpha = 4.24 \times 10^{-7}$ N m^{-1}. For the fluid phase, we consider the viscosity $\nu_0 = 1 \times 10^{-3}$ Pa s. We consider a constant flow rate, which is realized by applying a time-dependent force term $\boldsymbol{F} = (1/Fr(t), 0)^{\mathrm{T}}$, where Fr denotes the Froude number. If the current flow rate $Q(t)$ is lower or greater than the desired flow rate Q_0, we increase the force term by multiplying it with the ratio of Q_0/Q_t. The initial force term can be estimated from its Newtonian value: $1/Fr\ (t = 0) = 12Q_0/(h_l^3 Re)$, where h_l is the channel height. We choose $Q_0 = 15$

Symbol	Description	Value
L	Radius of a perimeter-equivalent circular cell	5×10^{-6} m
U	Characteristic velocity	2.25×10^{-5} m s^{-1}
ρ	Fluid density	10^{3} kg m^{-3}
ν_0	Dynamic viscosity of the fluid	10^{-3} Pa s
ν_{RBC}	Dynamic viscosity of the RBC	10^{-3} Pa s
ν_{WBC}	Dynamic viscosity of the WBC	5×10^{-2} Pa s
$b_{N,RBC}$	Bending rigidity of the RBC	2×10^{-19} J
$b_{N,WBC}$	Bending rigidity of the hard WBC	2×10^{-18} J
$b_{N,WBC}$	Bending rigidity of the soft WBC	2×10^{-19} J
ϵ	Diffuse interface thickness	0.04
γ	Regularization parameter	10^{-7}
α	Repulsion parameter	8.44×10^{-4} N m^{-1}

TABLE 1. Mechanical and numerical parameters used in the simulations. Mechanical parameters correspond to the considered values in Fedosov *et al.* (2012) and Takeishi *et al.* (2014).

for all simulations, which implies an averaged velocity of 8.44×10^{-5} m s^{-1} for all simulations and thus allows us to compare the results for different settings. An overview of all used parameters is given in table 1.

In non-dimensional units, the computational domain becomes $\Omega = [0, 8] \times [0, 4]$, with periodic boundary conditions in the x_1 direction. The WBC has the radius 1 and is put at (5, 2). RBCs are placed randomly such that they do not overlap. The non-dimensional numbers read $Re = 1.125 \times 10^{-4}$, $Be_{RBC} = 5.3$, $Be_{WBC} = 0.53$ (hard), $Be_{WBC} = 5.3$ (soft), $In = 0.1$ and $Fr(t = 0) = 4 \times 10^{-5}$. In x_2 direction we specify the Dirichlet conditions $\phi_i = -1$ for $i = 1, \ldots, n$, which ensures that all cells stay within the computational domain.

We first vary the deformability of the WBC and keep $H_t = 0.293$ constant. The results are presented in figure 2, where the lower left diagram shows the x_2 coordinate of the trajectory of the midpoint of the WBC. After an initial phase, the WBC moves towards the wall, but only the rigid WBC can attach to the wall, while the soft WBC moves away after a certain time. The lower right diagram shows the probability that the midpoint of the cell is within the upper part of the channel with height 0.1. The results nicely confirm the findings in Fedosov *et al.* (2012), that WBC margination is high for rigid cells and decreases for softer cells.

The second test concerns the influence of H_t. We vary the number of RBCs, which lead to different values of H_t, ranging from 0.098 to 0.39. Figure 3 shows the obtained results for a rigid WBC and figure 4 for a hard one.

For a rigid WBC, margination can be observed for all considered H_t. However, our simulations show a lower tendency to move to the wall for the smallest value of $H_t = 0.098$ and the largest tendency for $H_t = 0.195$ and $H_t = 0.293$. For the highest value $H_t = 0.39$, the probability slightly decreases. It seems more likely that due to the larger number of RBCs, interaction between WBC and RBCs are also possible close to the wall, which moves the WBC away from the wall, see $t = 10$, $t = 22$ and $t = 30$. This results give evidence for a decreasing WBC margination for high H_t, as also observed in Fedosov *et al.* (2012). In the case of a hard WBC, the cell remains in the centre and in contrast to figure 3, no margination occurs for the lowest H_t considered. Increasing H_t leads to WBC margination. However, contact with the wall

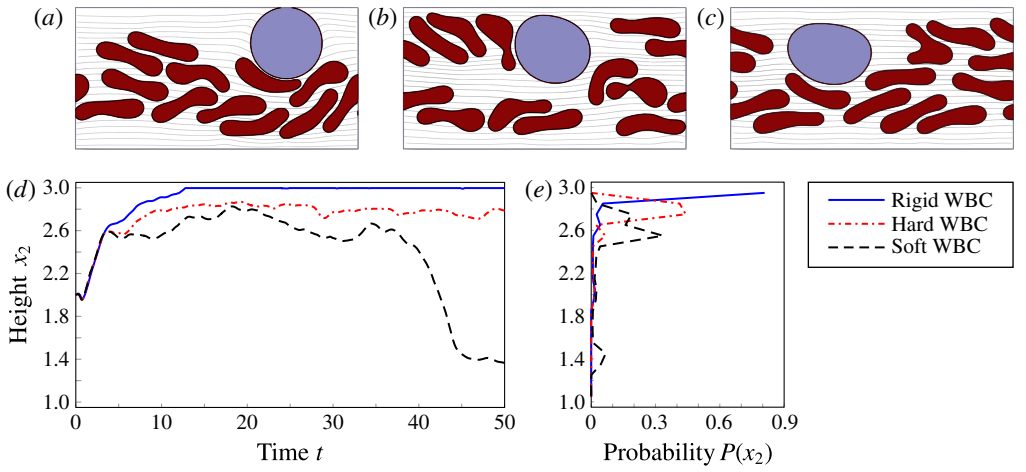

FIGURE 2. (Colour online) Simulation snapshot at late time for $H_t = 0.293$ for rigid, hard and soft WBC (a–c), x_2 coordinate for the trajectory of the midpoint of the WBC (e) and the probability that the midpoint of the WBC is inside a defined interval (d). The x_2 axis is split into 20 intervals of length 0.1.

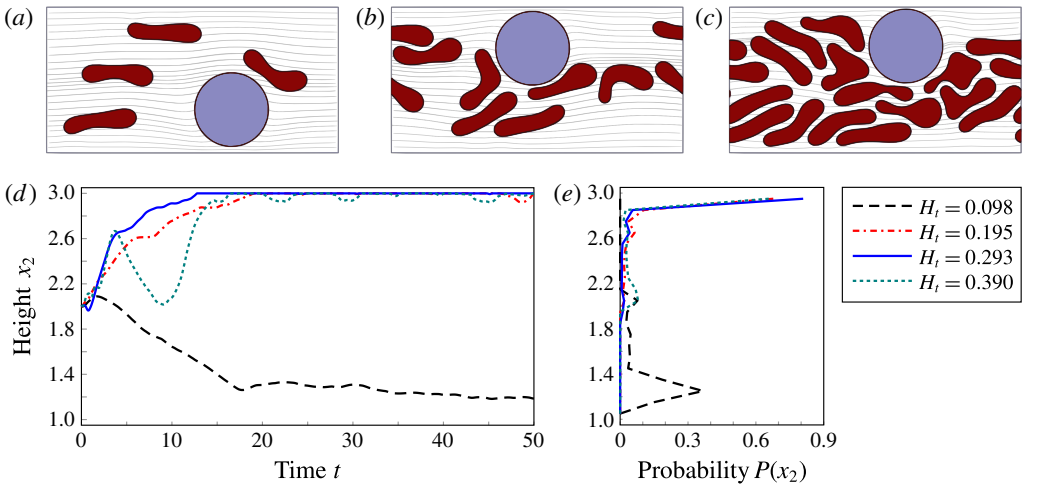

FIGURE 3. (Colour online) Simulation snapshot at late time for a rigid WBC for $H_t = 0.098$, $H_t = 0.195$ and $H_t = 0.39$ (a–c) ($H_t = 0.293$ is shown in figure 2). The x_2 coordinate for the trajectory of the midpoint of the WBC (e) and the probability that the midpoint of the WBC is inside a defined interval (d). The x_2 axis is split into 20 intervals of length 0.1.

cannot be achieved. We also do not see the tendency for decreasing WBC margination for $H_t = 0.39$. Further increasing $b_{N,WBC}$ or H_t is not possible due to numerical reasons.

So far, only already known results have been reproduced by the hydrodynamic phase field model, which can be viewed as a validation of the modelling approach. We now turn to the effect of the Reynolds number on WBC margination. It is shown in figure 5. We consider $H_t = 0.293$ and a rigid WBC. Considering a constant flow rate, we obtain WBC margination for $Re = 1.125 \times 10^{-4}$, $Re = 0.05$ and $Re = 1$. However,

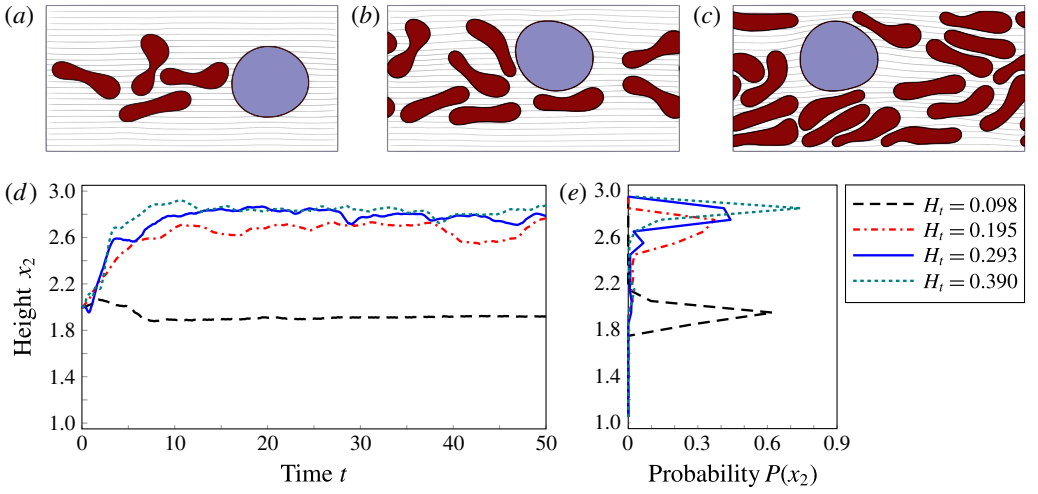

FIGURE 4. (Colour online) Simulation snapshot at late time for a hard WBC for $H_t = 0.098$, $H_t = 0.195$ and $H_t = 0.39$ (*a–c*) ($H_t = 0.293$ is shown in figure 2). The x_2 coordinate for the trajectory of the midpoint of the WBC (*e*) and the probability that the midpoint of the WBC is inside a defined interval (*d*). The x_2 axis is split into 20 intervals of length 0.1.

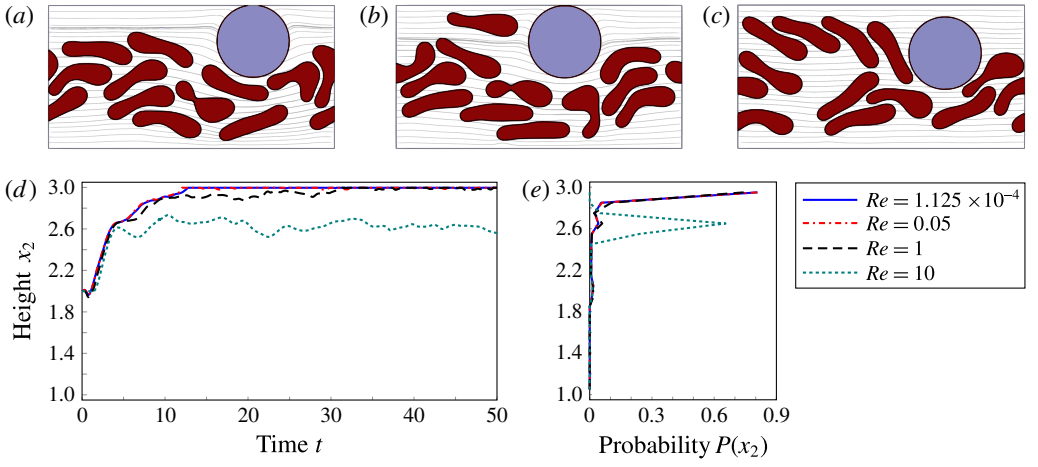

FIGURE 5. (Colour online) Simulation snapshot at late time for a rigid WBC and $H_t = 0.293$ for $Re = 0.05$, $Re = 1$ and $Re = 10$ (*a–c*) ($Re = 1.125 \times 10^{-4}$ is shown in figure 2). The x_2 coordinate for the trajectory of the midpoint of the WBC (*e*) and the probability that the midpoint of the WBC is inside a defined interval (*d*). The x_2 axis is split into 20 intervals of length 0.1. For $Re = 0.05$ a movie is provided in the online supplementary material available at http://dx.doi.org/10.1017/jfm.2016.15.

the tendency to adhere entirely decreases already for $Re = 1$. The simulation results for $Re = 10$ indicate no margination.

Various explanations can be given. First, the tendency of RBCs to aggregate in the centre of the vessel might decrease with increasing Re due to the increased

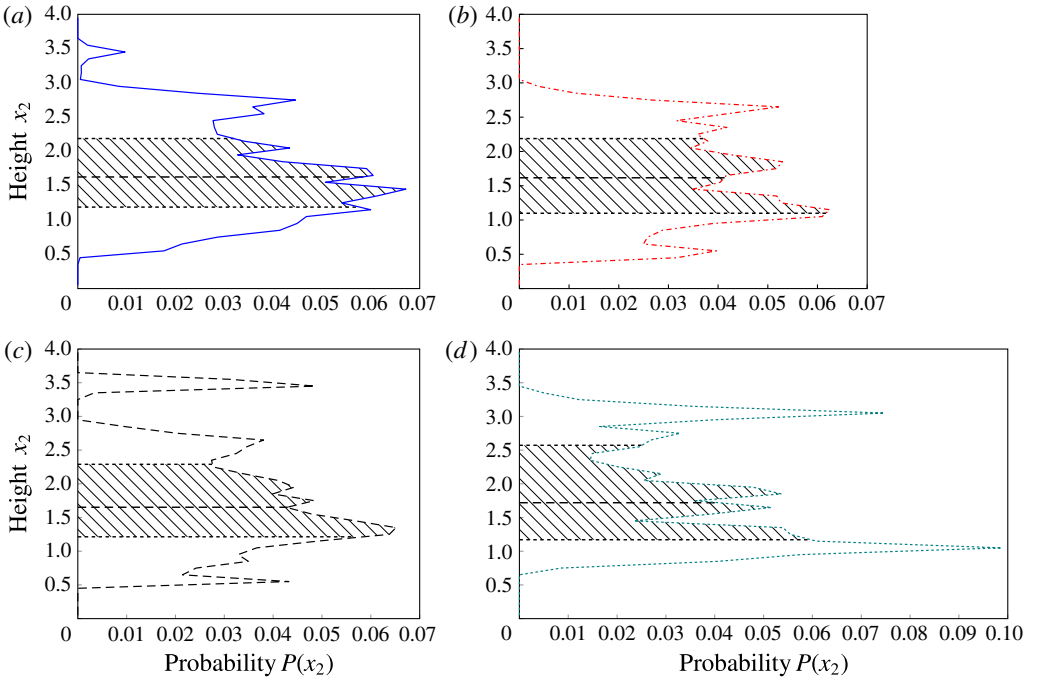

FIGURE 6. (Colour online) Distribution of RBCs for different Re, (*a*) 1.125×10^{-4}, (*b*) 0.05, (*c*) 1 and (*d*) 10, computed over the time interval $t = 10$ to $t = 50$. The shaded region shows the interquartile range, the difference between the upper and lower quartiles together with the median.

hydrodynamic interactions. This would increase the concentration of RBCs near the wall and thus lead to a stronger interaction with marginated WBCs, which, similar to the situation for large H_t, limits the time WBCs spend near the wall. However, this explanation cannot be justified by our numerical results. Figure 6 shows the distribution of RBCs in the vessel averaged over the simulation time, which does not, or only very weakly show a dependency on Re. The median is shifted towards the lower part due to the presence of the WBC in the upper part. The peak in the distribution for $Re = 1$ and $Re = 10$ in the upper part close to the wall results from RBCs, which are trapped behind the WBC, see figure 5. The lower half of the vessel thus gives a clearer description of the distribution, with no clear dependency on Re. This is in agreement with the results of Krüger, Kaoui & Harting (2014), where a qualitative similar distribution profile is observed for a suspension of soft capsules. Up to $Re = 50$ the profile shows no dependency on Re, but for larger Re the soft capsules are even strongly concentrated in the central region.

The second attempt considered the effect of Re on the lift force directly. The investigation of inertial forces on rigid particles dates back to Segre & Silberberg (1961) and its dependency on Re is today well understood for spherical objects (Ho & Leal 1974; Schonberg & Hinch 1989; Asmolov 1999; Matas, Morris & Guazzelli 2004; Carlo *et al.* 2009). For deformable objects this is much less investigated. Krüger *et al.* (2014) show that the Segre–Silberberg effect is essentially suppressed for deformable objects. We here consider the effect numerically and compute the lift force (density) as a function of Re for different cell types. We thereby follow the

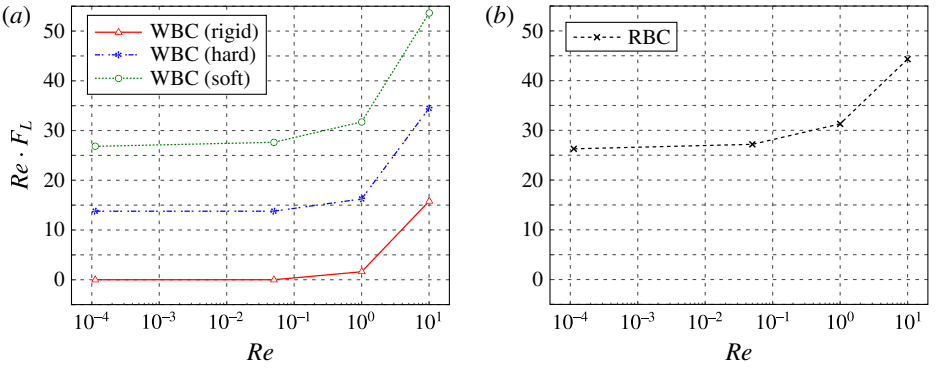

FIGURE 7. (Colour online) Computed lift force (density) for a WBC (*a*) and an RBC (*b*) as a function of Re.

approach in Meßlinger *et al.* (2009) and adapt a gravitational force $\boldsymbol{F}_g$ acting on the cell. In the hydrodynamic phase field models (2.23) and (2.25) this is realized by adding $-((\phi_i + 1)/2)\boldsymbol{F}_g$ to the right-hand side. The strength of $\boldsymbol{F}_g$ is varied to achieve a balance at a fixed height, which is chosen such that the lowest point of the cell is at $x_2 = 0.2$. Due to the strong deformability of the cell the usually used centre of mass position of the cell is not appropriate to achieve comparable results for the same cell type. The magnitude of $\boldsymbol{F}_g$ now determines the lift force (density) at position $x_2 = 0.2$. Figure 7 shows the computed values for WBCs (considered as rigid, hard and soft cells) and RBCs as a function of Re. We observe an increase of the lift force (density) with an increasing Re for all cell types. The increase is strongest for the soft WBC. However, also the increase of the lift force for the hard and rigid WBC is significant and explains the decrease in margination for an increasing Re, as now both cell types feel a lift force and thus compete for a position away from the vessel wall. However, to quantify this effect is difficult, as the computed values for WBCs and RBCs are not directly comparable, as the actual lift force depends on cell size, viscosity and distance from the vessel wall (Meßlinger *et al.* 2009), which all differ for WBCs and RBCs. However, the larger size of the WBCs and their higher viscosity indicate a stronger increase of the lift force with Re if compared with RBCs.

4. Conclusion

We investigate margination of WBCs using a hydrodynamic phase-field approximation of a Helfrich-type curvature-elastic model (Helfrich 1973). For RBCs various constraints concerning membrane inextensibility and area conservation are considered, while WBCs are modelled using a rigid body approximation or a Helfrich-type curvature model with a weakly extensible membrane. We also consider cell–cell interactions. The fluid flow of the blood plasma and the internal fluids of the cells are modelled using the incompressible Navier–Stokes equations. An idealized two-dimensional blood vessel is used as computational domain.

In the low-Re regime we have reproduced previous results, e.g. a decreasing tendency for margination with increasing deformability and a non-monotonic dependency on hematocrit, which quantitatively agree with results of Fedosov *et al.* (2012). Here the non-inertial lift force of WBCs is much lower than that on RBCs, or

even zero in the limit of a rigid-body approximation. This results in margination of the WBCs to the RBC-free layer near the wall. With inertia effects the simulations show a decreasing tendency for margination with increasing *Re*. The effect is explained by analysing the lift force on a single WBC and a single RBC as a function of *Re*. We now have an additional inertial lift force, which for all cell types increases if *Re* increases. This is also true for the hard and even the rigid WBC. These forces lead to a competition between WBCs and RBCs for a position away from the vessel wall, which suppresses margination. Due to the huge parameter space, flow confinement, deformability of the WBCs, haematocrit and inertia effects, we had to restrict our simulations to specific combinations, which show the most significant effect on WBC margination.

Acknowledgements

Simulations were carried out at ZIH at TU Dresden and JSC at FZ Jülich. W.M. and A.V. acknowledge support from the German Research Foundation through grant no. Vo-899/11. S.A. acknowledges support from the the German Research Foundation through grant no. Al-1705/1. We further acknowledge support from the European Commission within FP7-PEOPLE-2009-IRSES PHASEFIELD and computing resources at JSC through grant no. HDR06.

Supplementary movie

Supplementary movie is available at http://dx.doi.org/10.1017/jfm.2016.15.

REFERENCES

ABBITT, K. B. & NASH, G. B. 2003 Rheological properties of the blood influencing selectin-mediated adhesion of flowing leukocytes. *Am. J. Physiol. Heart Circ. Physiol.* **285**, H229–H240.

ALAND, S., EGERER, S., LOWENGRUB, J. & VOIGT, A. 2014 Diffuse interface models of locally inextensible vesicles in a viscous fluid. *J. Comput. Phys.* **277**, 32–47.

ASMOLOV, E. S. 1999 The inertial lift on a spherical particle in plane Poiseuille flow at large Reynolds number. *J. Fluid Mech.* **381**, 63–87.

BARK, D. L. & KU, D. N. 2010 Wall shear over high degree stenoses pertinent to atherothrombosis. *J. Biomech.* **43**, 2970–2977.

BEAUCOURT, J., RIOUAL, F., SEON, T., BIBEN, T. & MISBAH, C. 2004 Steady to unsteady dynamics of a vesicle in a flow. *Phys. Rev.* E **69**, 011906.

BIBEN, T., KASSNER, KL. & MISBAH, C. 2005 Phase-field approach to three-dimensional vesicle dynamics. *Phys. Rev.* E **72**, 041921.

BIBEN, T. & MISBAH, C. 2003 Tumbling of vesicles under shear flow within an advected-field approach. *Phys. Rev.* E **67**, 031908.

BONITO, A., NOCHETTO, R. H. & PAULETTI, M. S. 2011 Dynamics of biomembranes: effect of the bulk fluid. *Math. Model. Nat. Phenom.* **6**, 25–43.

BRETHERTON, F. P. 1962 The motion of rigid particles in a shear flow at low Reynolds number. *J. Fluid Mech.* **14**, 284–304.

CAMPELO, F. & HERNÁNDEZ-MACHADO, A. 2007 Shape instabilities in vesicles: a phase-field model. *Eur. Phys. J. Special Topics* **143**, 101–108.

CARLO, D. DI, HUMPHRY, E. J., STONE, H. & TONER, M. 2009 Particle segregation and dynamics in confined flows. *Phys. Rev. Lett.* **102**, 094503.

DU, Q., LI, M. & LIU, C. 2007 Analysis of a phase field Navier–Stokes vesicle–fluid interaction model. *J. Discrete Continuous Dyn. Syst.* B **8**, 539–556.

DU, Q., LIU, C., RYHAM, R. & WANG, X. 2005 A phase field formulation of the Willmore problem. *Nonlinearity* **18**, 1249–1267.

DU, Q., LIU, C. & WANG, X. 2006 Simulating the deformation of vesicle membranes under elastic bending energy in three dimensions. *J. Comput. Phys.* **212**, 757–777.

FEDOSOV, D. A., FORNLEITNER, J. & GOMPPER, G. 2012 Margination of white blood cells in microcapillary flow. *Phys. Rev. Lett.* **108**, 028104.

FEDOSOV, D. A. & GOMPPER, G. 2014 White blood cell margination in microcirculation. *Soft Matt.* **10**, 2961–2970.

FISCHER, T. M., STÖHR-LIESEN, M. & SCHMID-SCHÖNBEIN, H. 1978 The red-cell as a fluid droplet: tank tread-like motion of the human erythocyte-membrane in shear flow. *Science* **202**, 894–896.

FORMAGGIAM, L., QUARTERONI, A. & VENEZIANI, A. 2000 *Cardiovascular Mathematics: Modeling and Simulation of the Circulatory System*. Springer.

FREUND, J. B. 2007 Leukocyte margination in a model microvessel. *Phys. Fluids* **19** (2), 023301.

GEISLINGER, T. M. & FRANKE, T. 2014 Hydrodynamic lift of vesicles and red blood cells in flow – from Fåhraeus & Lindqvist to microfluidic cell sorting. *Adv. Colloid Interface Sci.* **208**, 161–176.

GHIGLIOTTI, G., BIBEN, T. & MISBAH, C. 2010 Rheology of a dilute two-dimensional suspension of vesicles. *J. Fluid Mech.* **653**, 489–518.

GOLDSMITH, H. L. & MASON, S. G. 1961 Axial migration of particles in Poiseuille flow. *Nature* **190**, 1095–1096.

GU, R., WANG, X. & GUNZBURGER, M. 2014 Simulating vesicle–substrate adhesion using two phase field functions. *J. Comput. Phys.* **275**, 626–641.

HAUßER, F., LI, S., LOWENGRUB, J., MARTH, W., RÄTZ, A. & VOIGT, A. 2013 Thermodynamically consistent models for two-component vesicles. *Intl J. Biomath. Biostat.* **2** (1), 19–48.

HELFRICH, W. 1973 Elastic properties of lipid bilayers: theory and possible experiments. *Z. Naturforsch. c* **28**, 693–703.

HO, B. P. & LEAL, L. G. 1974 Inertial migration of rigid spheres in two-dimensional unidirectional flows. *J. Fluid Mech.* **65**, 365–400.

JAIN, A. & MUNN, L. L. 2009 Determinants of leukocyte margination in rectangular microchannels. *PLoS ONE* **4** (9), e7104.

KIM, Y. & LAI, M.-C. 2010 Simulating the dynamics of inextensible vesicles by the penalty immersed boundary method. *J. Comput. Phys.* **229**, 4840–4853.

KRAUS, M., WINTZ, W., SEIFERT, U. & LIPOWSKY, R. 1996 Fluid vesicle in shear flow. *Phys. Rev. Lett.* **77**, 3685–3688.

KRÜGER, T., KAOUI, B. & HARTING, J. 2014 Interplay of inertia and deformability on rheological properties of a suspension of capsules. *J. Fluid Mech.* **751**, 725–745.

KU, D. 1997 Blood flow in arteries. *Annu. Rev. Fluid Mech.* **29**, 399–434.

KUMAR, A. & GRAHAM, M. D. 2012 Margination and segregation in confined flows of blood and other multicomponent suspensions. *Soft Matt.* **8**, 10536–10548.

LAADHARI, A., SARAMITO, P. & MISBAH, C. 2012 Vesicle tumbling inhibited by inertia. *Phys. Fluids* **24**, 031901.

LING, S., MARTH, W., PRAETORIUS, S. & VOIGT, A. 2015 An adaptive finite element multi-mesh approach for interacting deformable objects in flow. *Comput. Meth. Appl. Math.* doi:10.1515/cmam-2016-0003.

MARTH, W. & VOIGT, A. 2014 Signaling networks and cell motility: a computational approach using a phase field description. *J. Math. Biol.* **69**, 91–112.

MATAS, J.-P., MORRIS, J. F. & GUAZZELLI, E. 2004 Inertial migration of rigid spherical particles in Poiseuille flow. *J. Fluid Mech.* **515**, 171–195.

MEßLINGER, S., SCHMIDT, B., NOGUCHI, H. & GOMPPER, G. 2009 Dynamical regimes and hydrodynamic lift of viscous vesicles under shear. *Phys. Rev.* E **80**, 011901.

N'DRI, N. A., SHYY, W. & TRAN-SON-TAY, R. 2003 Computational modeling of cell adhesion and movement using a continuum-kinetics approach. *Biophys. J.* **85**, 2273–2286.

PEARSON, M. J. & LIPOWSKY, H. H. 2000 Influence of erythrocyte aggregation on leukocyte margination in postcapillary venules of rat mesentery. *Am. J. Physiol. Heart Circ. Physiol.* **279**, H1460–H1471.

PROTHERO, J. W. & BURTON, A. C. 1962 The physica of blood flow in capillaires. *Biophys. J.* **2**, 199–212.

SALAC, D. & MIKSIS, M. J. 2011 A level set projection model of lipid vesicles in general flows. *J. Comput. Phys.* **230**, 8192–8215.

SALAC, D. & MIKSIS, M. J. 2012 Reynolds number effects on lipid vesicles. *J. Fluid Mech.* **711**, 122–146.

SCHONBERG, J. & HINCH, E. 1989 Inertial migration of a sphere in Poiseuille flow. *J. Fluid Mech.* **203**, 517–524.

SEGRE, G. & SILBERBERG, A. 1961 Radial particle displacements in Poiseuille flows of suspensions. *Nature* **189**, 209–210.

SOHN, J. S., TSENG, Y.-H., LI, S., VOIGT, A. & LOWENGRUB, J. 2010 Dynamics of multicomponent vesicles in a viscous fluid. *J. Comput. Phys.* **229**, 119–144.

TAKEISHI, N., IMAI, Y., NAKAAKI, K., YAMAGUCHI, T. & ISHIKAWA, T. 2014 Leukocyte margination at arteriole shear rate. *Physiol. Rep.* **2**, e12037.

TANAKA, H. & ARAKI, T. 2000 Simulation method of colloidal suspensions with hydrodynamic interactions: fluid particle dynamics. *Phys. Rev. Lett.* **85**, 1338–1341.

VEERAPANENI, S. K., GUEYFFIER, D., ZORIN, D. & BIROS, G. 2009 A boundary integral method for simulating the dynamics of inextensible vesicles suspended in a viscous fluid in 2D. *J. Comput. Phys.* **228**, 2334–2353.

VENNEMANN, P., LINDKEN, R. & WESTERWEEL, J. 2007 In vivo whole-field blood velocity measurement techniques. *Exp. Fluids* **42**, 495–511.

VEY, S. & VOIGT, A. 2007 AMDiS: adaptive multidimensional simulations. *Comput. Visual. Sci.* **10**, 57–67.

WITKOWSKI, T., LING, S., PRAETORIUS, S. & VOIGT, A. 2015 Software concepts and numerical algorithms for a scalable adaptive parallel finite element method. *Adv. Comput. Math* **41**, 1145–1177.

ZHANG, J., DAS, S. & DU, Q. 2009 A phase field model for vesicle–substrate adhesion. *J. Comput. Phys.* **228**, 7837–7849.

ZHAO, H. & SHAQFEH, E. S. G. 2011 The dynamics of a vesicle in simple shear flow. *J. Fluid Mech.* **674**, 578–604.